JOURNAL OF NANOMATERIALS AND DEVICES
Jul - Dec 2023, VOL. 1, ISSUE 1
https://doi.org/10.61577/jnd.2023.100002

RESEAPRO JOURNALS

ORIGINAL ARTICLE

OPEN ACCESS

TiO_2 nanoparticles synthesized sonochemically: its electrochemical lead sensor and photocatalytic degradation of DG and F-OR dyes

D.A. Raghupathy[1,2], G. Ramgopal[3], N. Raghavendra[4], C.R. Ravikumar[4], H.C. Ananda Murthy[5,6]

[1]Department of Physics, Dr. Ambedkar Institute of Technology, Bangalore, India
[2]Bharathiar University, Coimbatore, Tamilnadu, India
[3]Department of Physics, Maharani's Science College for Women, Maharani Cluster University, Bengaluru, India
[4]Department of Science, East West Institute of Technology, VTU, Bangalore, India
[5]Department of Applied Chemistry, School of Applied Natural Science, Adama Science and Technology University, Adama, Ethiopia
[6]Department of Prosthodontics, Saveetha Dental College and Hospital, Saveetha Institute of Medical and Technical Science, Saveetha University, Tamil Nadu, India

ABSTRACT

Sonochemical synthesis of titanium oxide nanoparticles (TONPs) was done at a low cost. Powder X-ray diffraction (PXRD) investigation has verified that the average TiO_2 crystallite size was 39.42 nm. Diffuse reflectance spectroscopy (DRS) by the Kubelka-Monk function was used to confirm the average energy gap of TiO_2 NPs (3.26 eV). TONPs have been successfully used with inventive photocatalysts to remove the dyes Direct green (DG) and Fast orange-red (F-OR). Direct Green (DG) and Fast Orange Red (F-OR) dyes were used as conventional dyes to investigate the photocatalytic properties of NPs under UV light and sunlight irradiation. Fast orange-red dye is excited at 498.59 nm and 489.20 nm, while Direct green dye was discovered to be stimulated at 609.7 nm and 613.3 nm under UV and sunlight. Using carbon paste electrodes in 0.1N HCl solution, cyclic voltammetry (CV) was used to examine the electrochemical characteristics of the produced sample. The TiO_2 electrode that was produced could detect lead in an acidic solution. The TiO_2 electrode is a promising electrode material for making sensor applications because of its higher electrochemical behavior.

KEYWORDS

TiO_2 nanoparticles; Energy gap; Direct green; Fast orange red; Electrochemical Sensor

ARTICLE HISTORY

Received: 26 July 2023; Revised: 21 September 2023; Accepted: 25 September 2023

Introduction

Many different types of metal and metal oxide nanoparticles have been used in physical and chemical processes. Despite the fact that these systems have produced a large number of incredibly varied nanostructures, various environmental toxicity problems have surfaced [1]. Due to the enormous variety of structural, material, and functional characteristics displayed by their nanoparticles, metal oxides have recently received a lot of attention. Due to their unique characteristics when compared to the respective bulk metals, transition metal oxide nanoparticles have attracted a lot of scientific attention. They also have a wide range of industrial applications [2]. Different synthetic methods have been used to create metal oxide nanoparticles with various morphologies and sizes. These include wet-chemical, hydrothermal, solvothermal, microwave, and vapor deposition techniques [3-5]. In the environmentally friendly process of photocatalysis, light energy is transformed into chemical energy in an environment-friendly manner. Environmental organic pollutants are mostly produced by the textile and paint industries, and solar-driven photocatalytic systems have demonstrated excellent performance in resolving environmental issues in recent years.

Therefore, it is crucial that the latter is broken down and transformed into safe mineral compounds. The photocatalyst can be used for environmental remediation, which includes the removal of organic pollutants from the air and the abstraction of pesticides, fungicides, and fertilizers from wastewater [6]. A semiconductor photocatalyst is activated by the absorption of a photon, which causes the production of a hole (h^+) in the valence band and the transfer of an electron from the valence band to the conduction band. Any contaminants that are adsorbed onto the photocatalyst surface will undergo reduction or oxidation by the electron-hole pair, respectively, as a result of these photo-generated charge carriers. In photocatalysis, the metal oxide photocatalyst surface typically serves as an active centre by producing either OH radicals (by oxidizing OH^- anions) or O_2 radicals (by the reduction of O2) [7-12].

The organic pollutants that have been adsorbed then undergo a reaction with these photo-generated radicals and anions, decomposing or mineralizing them into less hazardous byproducts. Highly dangerous substances can be converted into less harmful or non-toxic products like CO_2 and H_2O using the photocatalytic reaction [13,14]. Metal oxides can therefore be used as excellent candidates for the efficient photocatalytic destruction of environmental pollutants. The green synthesis of titanium oxide nanoparticles (TONPs) and their efficient usage in the photocatalytic degradation of two commonly used organic dyes, Direct green (DG) and Fast orange red (FOR), have been the main topics of this study.

In the present work, nanosized TiO_2 is synthesized using a simple sonochemical method in a deoxygenated

*Correspondence: H.C. Ananda Murthy, Department of Applied Chemistry, School of Applied Natural Science, Adama Science and Technology University, PO Box 1888, Adama, Ethiopia, e-mail: anandkps350@gmail.com

environment, without the need of any surfactants. The structural, chemical composition, optical, photocatalytic, and sensor studies of the NPs were also carried out using X-ray diffraction (XRD), Fourier transform infrared spectroscopy (FT-IR), transmission electron microscopy (TEM), diffusion reflectance spectroscopy (DRS), cyclic voltammetry (CV), and electrochemical impedance studies (EIS).

Material and Methods

Problem analysis

The probe sonication technique was utilized to synthesize TONPs from the precursors cupric nitrate ($Ti(NO_3)_4$) and sodium hydroxide (NaOH). TONPs were synthesized by adding a 0.5M solution of sodium hydroxide dropwise to a 1M solution of titanium nitrate in a beaker volume of 250 ml and aggressively stirring the mixture until precipitation was achieved. After the combined solution was sonicated for one hour at a temperature of 45 °C with an ultrasonic pulse of 30 ± 2 kHz, a gelatinous white precipitate was formed. After repeatedly washing it with demineralized water, filter the precipitate that has formed. TONPs were created by annealing the precipitate for two hours at 600 °C following an hour-long dehydration period at 100 °C in a hot air chamber.

$$Ti(NO_3)_4+4NaOH \rightarrow Ti(OH)_4\downarrow+4NaNO_3 \quad (1)$$
$$Ti(OH)_4\rightarrow TiO(OH)_2\downarrow+H_2O \quad (2)$$
$$TiO(OH)_2\rightarrow TiO_2+H_2O \quad (3)$$

Characterizations

The phase structure and crystalline nature of TiO_2 NPs were investigated by XRD utilizing a nickel filter and a Shimadzu PXRD-7000 X-ray diffractometer with CuK radiation (λ =1.541 Å). With KBr pellets ranging in size from 400 to 4000 cm^{-1}, FTIR analyses of the samples were carried out using a Perkin Elmer Spectrum-1000 FTIR Spectrophotometer. Elico SL- 150 spectrophotometer was used to study the samples using UV-Visible spectrophotometer in the 200-800 nm range. The CV measurement was performed using a tri-electrode setup with a carbon paste electrode, platinum wire, and Ag/AgCl as the working, counter, and reference electrodes, respectively, and a 0.1N HCl solution as the electrolyte on an electrochemical analyzer (CHI608E potentiostat).

Preparation of Carbon paste electrode

The prepared sample (TONPs), graphite powder, and silicon oil were manually combined in an agate mortar for around 30 minutes at a mass ratio of 15:70:15 to create the carbon paste electrode. A handmade Teflon cavity tube was then filled with the resulting paste. On a piece of weighing paper, the packed carbon paste's surface was smoothed [15].

Results and Discussions

PXRD analysis

The PXRD patterns of the TONPs are depicted in Figure 1. The diffraction peaks at 2θ = 25.40, 38.14, 48.15, 54.02, 55.04, and 62.70 that were assigned to the (101), (004), (200), (105), (211), (204), (116), and (220) planes, respectively, are in good agreement with JCPDS card No. 78-2486, which confirms the anatase phase of TiO_2 [16]. The crystallite size (D) of the calcined samples was discovered to be between 37 and 40 nm using the Debye Scherrer's technique and the full width half-maximum (FWHM) of the powder diffraction peak.

$$D = \frac{K\lambda}{\beta \cos\theta} \quad (4)$$

Where,
D = crystallite size,
K = 0.9~diffraction constant (shape factor),
λ = 1.54 (X-Ray source wavelength),
β = full width at half maximum intensity (FWHM) in radians and
θ = angle of diffraction.

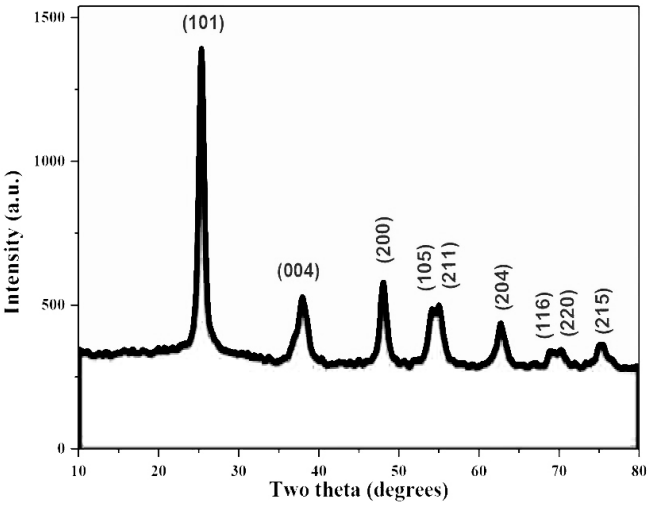

Figure 1. PXRD Patterns of TiO_2 NPs.

FT-IR analysis

A broad intense band at 3430 cm^{-1} in the spectra can be assigned to the N-H stretching frequency coming from the peptide linkages present in the proteins of the biosynthesis of a flavus employing TiO_2, according to FTIR investigations of the TONPs (Figure 2). Anhydride group's asymmetrical C-O linked (str.) vibration has a significant absorption peak at 1775 cm^{-1}. With the aid of FTIR, it was possible to spot changes in the carbonyl region (1600-1800 cm^{-1}), the emergence of distinctive bands at 1775 cm^{-1} and 1635 cm^{-1} that could be attributed to amide I and II, as well as a sharp decline in the relative intensity of the bands (representing the symmetric C-O stretching vibrations from maleic anhydride groups) [17].

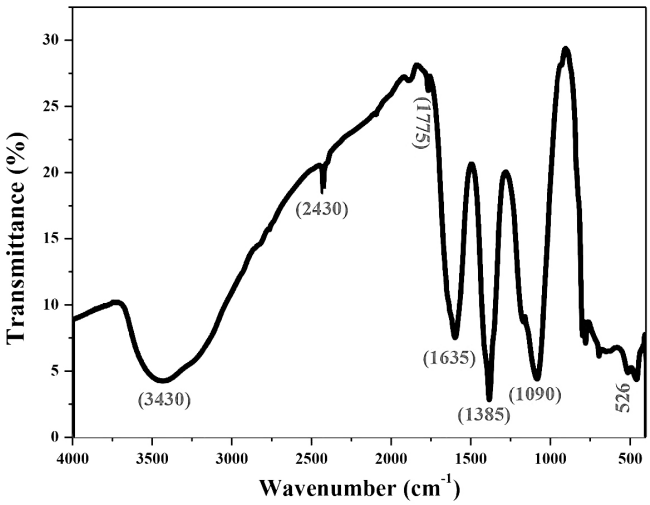

Figure 2. FTIR spectra of TONPs.

https://doi.org/10.61577/jnd.2023.100002

RESEAPRO JOURNALS

UV-DRS studies

Figure 3 shows the DRS and energy gap spectra (Inset) of TONPs. Plotting of the spectra is done using F(R), which is the same as the absorption coefficient. Divalent titanium ions have hexagonal-symmetric $3d^2$ electronic structures. Due to the hexagonal Ti^{4+} ions' spin-allowed d-d transitions, the main absorption bands were visible at 420 nm. The sample of powder scatters light widely and thickly, making it difficult to comprehend the absorption spectrum. To get over this challenging situation, equation (5) diffused reflectance and Schuster-Kubelka-Munk (SKM) connection are employed to link the diffused reflectance to the absorption coefficient needed for analyzing the powders [18].

$$F(R) = \frac{(1-R)^2}{2R} \qquad (5)$$

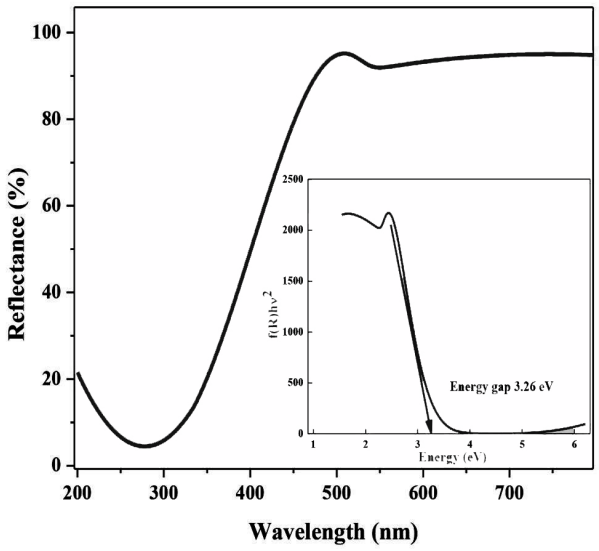

Figure 3. Diffuse reflectance spectra and Energy gap spectra (Inset) of TONPs.

The optical band gap of the produced sample communicates with electron excitation from the valence band to the conduction band and was determined using the Tauc relation as in equation (6), where R is the absolute reflectance of the sampled, and F(R) [19].

$$(R)\ h\nu = A\ (h\mathrm{h}\nu - \mathrm{Eg})^{n} \qquad (6)$$

Where A is a constant, hυ is the photon energy, n=2 for a direct allowed transition, and n=1/2 for an indirect allowed transition [20]. To obtain the direct band gap energy is 3.26 eV, the linear section of the curve was extrapolated to $(F(R)h)^2=0$. The band gap energy (Eg) value, which was determined from the plot and is depicted inset in Figure 3.

TEM analysis

Deep insights into the morphological characteristics of the TONPs have been gained by the effective usage of TEM-HRTEM-SAED technical micrographs and patterns. Figure 4a as-synthesized TONPs are generally spherical but also comprise both regular and asymmetric geometries, according to the TEM picture. The existence of nanoparticles with a size of 40 nm or less demonstrates the efficiency of the probe sonication method; otherwise, agglomerated particles would have formed. The NPs' crystallinity and the crystalline structure of the material are supported by the accompanying HRTEM image (Figure 4b) and Bright spots that appear on the SAED pattern of TONPs (Figure 4c), which are in line with the previously mentioned XRD data.

Photocatalytic analysis

A Shimadzu UV-visible spectrophotometer model 2600 was used to perform photocatalytic activities. In a photocatalytic experiment, the created TiO_2 NPs were utilized to degrade the selected dyes Direct Green-23 (DG-23) and F-OR in the presence of UV rays and sunlight illumination. Using 250 ml of dye solution at concentrations of 10, 15, 20, and 25 ppm, the dye stock solution was made. This dye solution was put into a

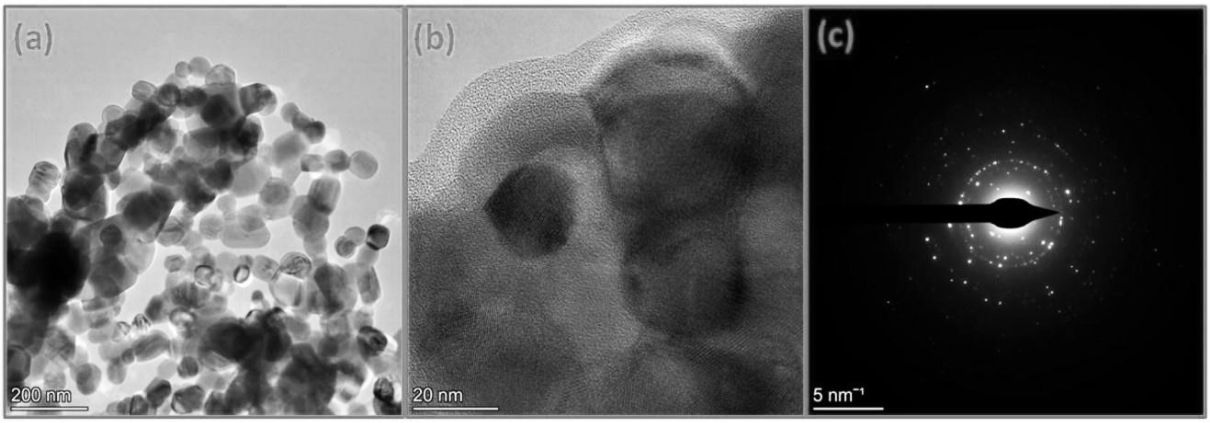

Figure 4. (a) TEM image (b) HRTEM and (c) SAED pattern of TONPs.

circular glass reactor along with 20, 30, 40, 50, and 60 mg of catalyst, respectively. The reaction mixture was stirred magnetically and illuminated by a 400-watt mercury vapour lamp with a 254 nm wavelength. The experiments were done in a Pyrex glass beaker. 5 mL of the sample solution was removed from the reaction mixture every 15 minutes for 120 minutes while being watched in the UV-visible range of 200-800 nm. The reaction mixture was exposed to UV light in the open air. The photocatalytic activity of TiO_2 NPs was proxied by the degradation of the DG and F-OR aqueous solutions [21-23]. On Oct 2nd, 2022 (Sunday), at 1:30 pm, in Bengaluru, the Natural Sunlight photocatalytic experiment was conducted using the same methodology. DG and F-OR dye solutions containing 20 ppm were given 60 mg of the catalyst. The generated dye solution was left in this state in the absence of light before the experiment started to maintain the balance

https://doi.org/10.61577/jnd.2023.100002

between adsorption and desorption. In the dark, the dye solution seems to deteriorate at a negligibly low rate (4%) After that, the dye was placed in the sun and subjected to UV rays for 120 minutes [24-26]. The photocatalytic activity of the TiO_2 nanoparticles was assessed using the photodegradation of DG, a cationic dye with maximal absorption at 609.7 nm and 613.3 nm under UV and sunlight, as shown in Figures 5a and 5b. An anionic dye called F-OR exhibits maximum UV and sunlight absorption at 498.59 nm and 489.20 nm, respectively (Figure 6a and 6b) [27,28]. The photodegradation rate of the DG dye decolorized to 88.9% in UV and 67.75% in sunlight after 120 minutes of exposure, while the photodegradation rate of the F-OR dye is 94.75% in UV and 83.75% in sunlight, respectively (Figure 7a and 7b). This reveals unequivocally that TiO_2 exhibits more photocatalytic action when acting as a catalyst to break down DG and F-OR dyes when exposed to UV light than sunlight. The significance of the fabrication method, crystal size, shape, and electron-hole recombination in the photocatalytic degradation of DG and F-OR dyes is highlighted by these results [29,30]. The degradation percentage of the dyes was calculated using equation (7).

$$\% \text{ degradation} = \frac{c_0 - c_e}{c_e} \times 100 \qquad (7)$$

Where C_0 is the initial dye concentration and C_e is the dye concentration after adsorption at time t seconds. Further, C/Co values were also calculated by the following equation (8).

$$\log \frac{c}{c_0} = -Kt \qquad (8)$$

Where Co and C are the dye concentrations at time t=0 minutes and the testing time, respectively, and k is the first order rate constant. The calculated data showed that log C/Co and k have a linear relationship, supporting first order kinetics. The slope k was calculated for DG under UV is 0.005418 $min^{-1}$and Sunlight is 0.004533 min^{-1}, F-OR under UV is 0.011144 min^{-1} and Sunlight is 0.006959 min^{-1}.

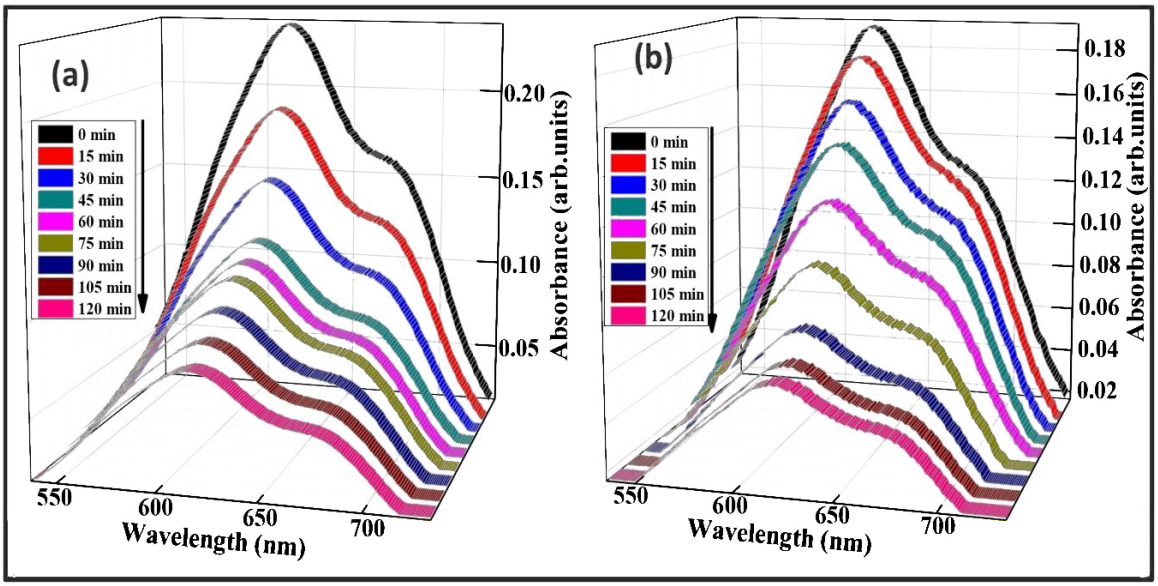

Figure 5. Spectral absorbance of TiO_2 photocatalyst for the decolorization of DG under UV and Sunlight illumination.

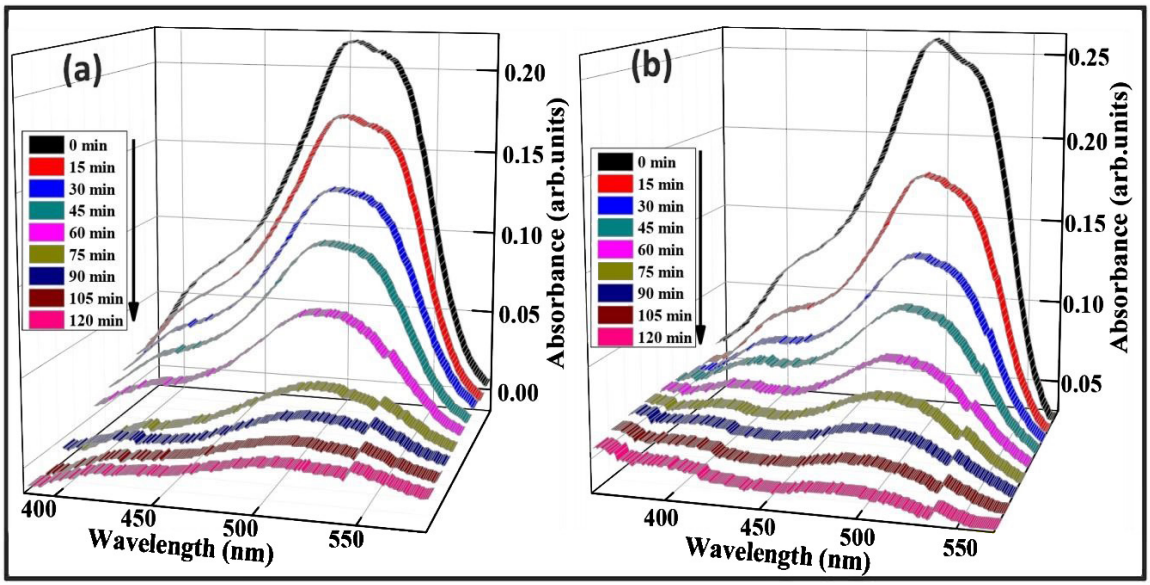

Figure 6. . Spectral absorbance of TiO_2 photocatalyst for the decolorization of F-OR under UV and Sunlight illumination.

https://doi.org/10.61577/jnd.2023.100002

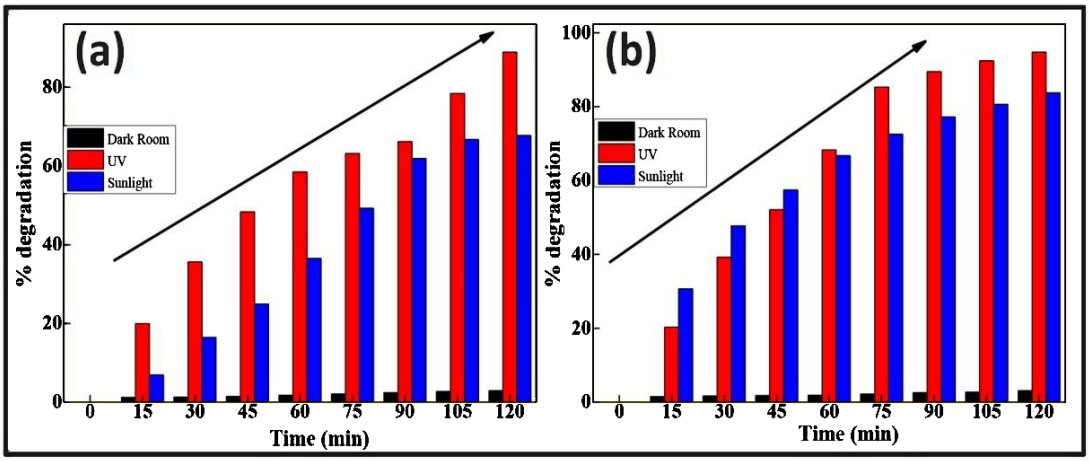

Figure 7. Percentage of decolorization of TiO_2 photocatalyst for the decolorization of DG and F-OR under UV and sunlight illumination.

The following outlines a potential mechanism for dye decolorization using photocatalyst TiO_2 exposed to UV and sunlight. As soon as UV and sunlight hit the material, the electrons in the valence band of TiO_2 NPs were stimulated to the conduction band, leaving the equal number of holes in the valence band behind. These photoinduced holes may directly interact with the dye, surface oxygen vacancies, or surface-bound water to produce a hydroxyl radical ($OH^{\bullet}$). While this is happening, superoxide radical ($O_2^{\bullet -}$) may form when electrons come into contact with outside oxygen [31-33]. This superoxide radical undergoes further interactions with H^+ to produce $HO_2^{\bullet}$, which combines with trapped electrons to produce more $OH^{\bullet}$.

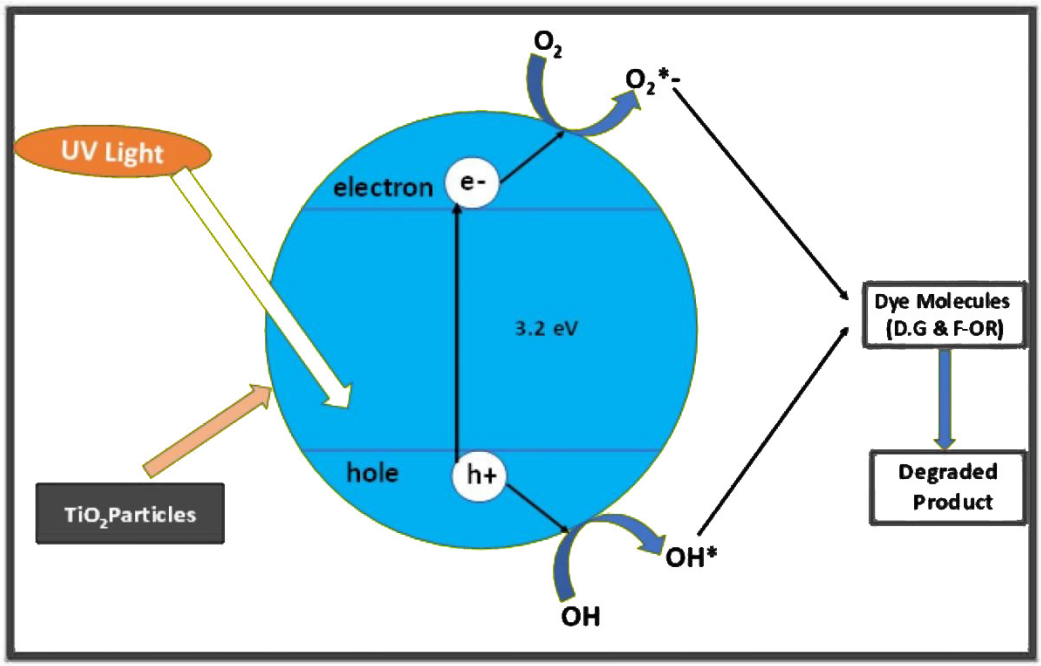

Figure 8. Schematic representation of dye degradation of TiO_2 photocatalyst on DG and F- OR dye under UV light.

The steps involved in the photocatalytic degradation process under UV–visible light irradiation are as follows

$$TiO_2 + h\nu \longrightarrow e^- + h^+ \quad (9)$$

$$O_2 + e^- \longrightarrow O_2^{\bullet} \quad (10)$$

$$OH + h^+ \longrightarrow OH^{\bullet} \quad (11)$$

$$O_2^{\bullet -} + OH^{\bullet} + \text{dye} \longrightarrow \text{degradation product} \quad (12)$$

As a result, as seen in Figures 8 and 9, the photo decolorization activity of dye is substantially determined by the amount of TiO_2 photocatalyst used. By adjusting the catalyst dose from 20 to 60 mg (20, 30, 40, 50, and 60 mg) while keeping a constant dye concentration of 20 ppm, the decolorization activity of DG and F-OR dyes was examined. According to Figures 10 and 11 (a,b), the rate of dye photodegradation increased after 120 minutes at the indicated catalyst concentration (60 mg) [34-36]. The effects of screening and light scattering may have contributed to the activity decreasing as the catalyst dosage was increased by an additional 60 mg. The concentration of dyes has been a major degradation in photocatalytic degradation in UV and sunlight. In order to establish the appropriate dye concentration, experimental techniques were employed to vary the DG and F-OR dye concentrations from 10 to 25 ppm (10,15, 20 and 25). As a result, the quantity of dye molecules that bind to the surface of the photocatalyst reduces as dye concentration rises. As shown in Figures 12 and 13 (a,b) [37,38], dye concentration demonstrates superior photo decolorization activities at 20 ppm.

https://doi.org/10.61577/jnd.2023.100002

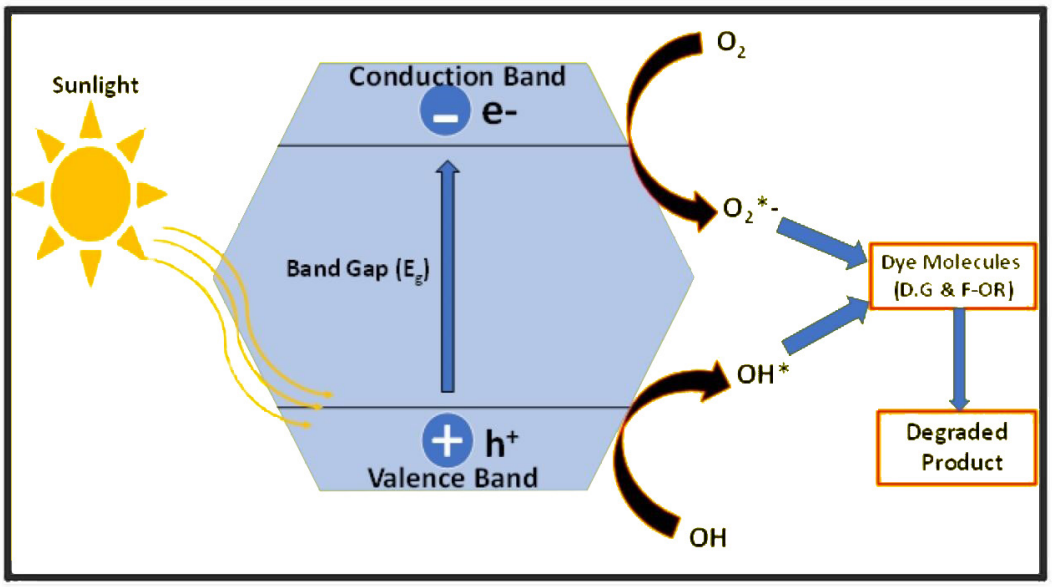

Figure 9. Schematic representation of dye degradation of TiO_2 photocatalyst on DG and F-OR dye under sunlight.

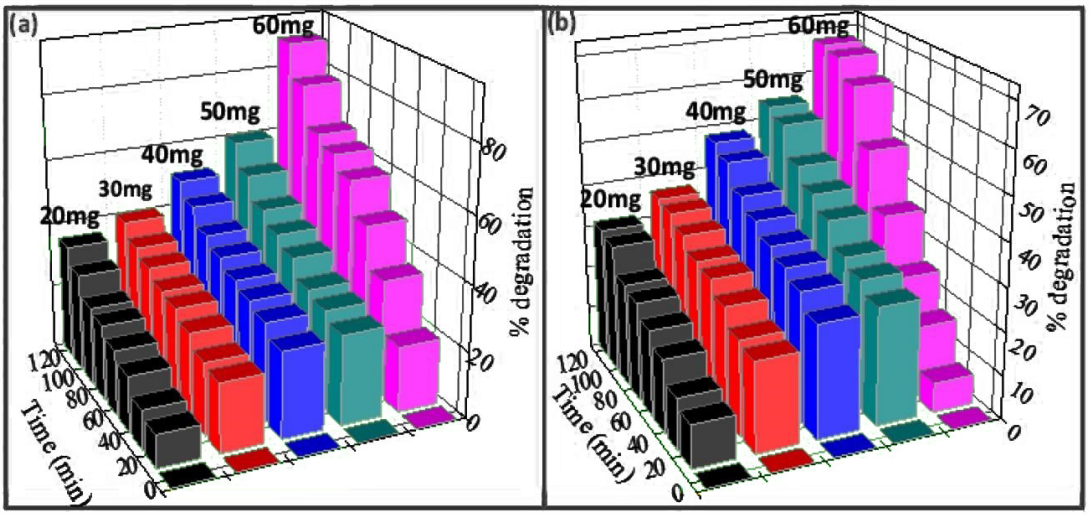

Figure 10. Rate of photodegradation for different dye concentration of TiO_2 photocatalyst for the decolorization of DG under UV and Sunlight illumination.

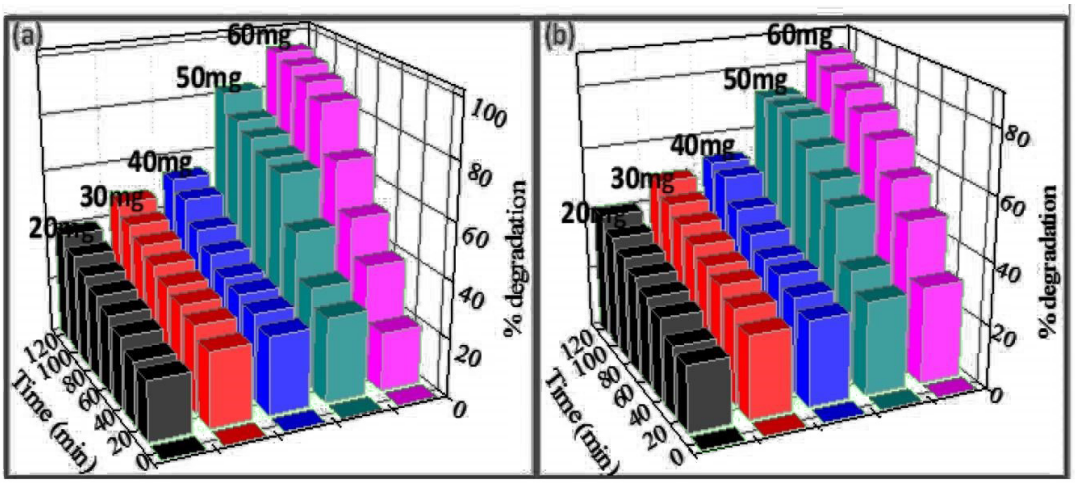

Figure 11. Rate of photodegradation for different dye concentration of TiO_2 photocatalyst for the decolorization of F-OR under UV and Sunlight illumination.

https://doi.org/10.61577/jnd.2023.100002

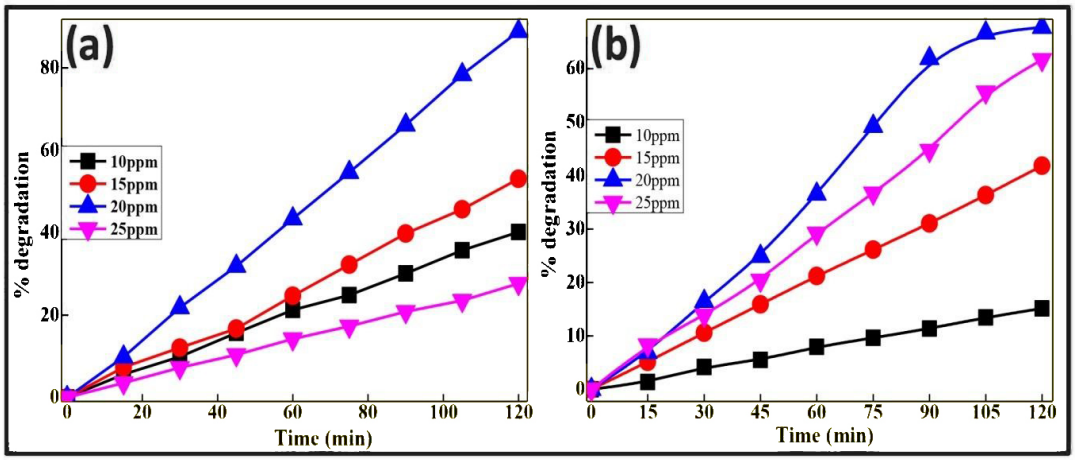

Figure 12. . Rate of photodegradation for different ppm of TiO_2 photocatalyst for the decolorization of DG under UV and Sunlight illumination.

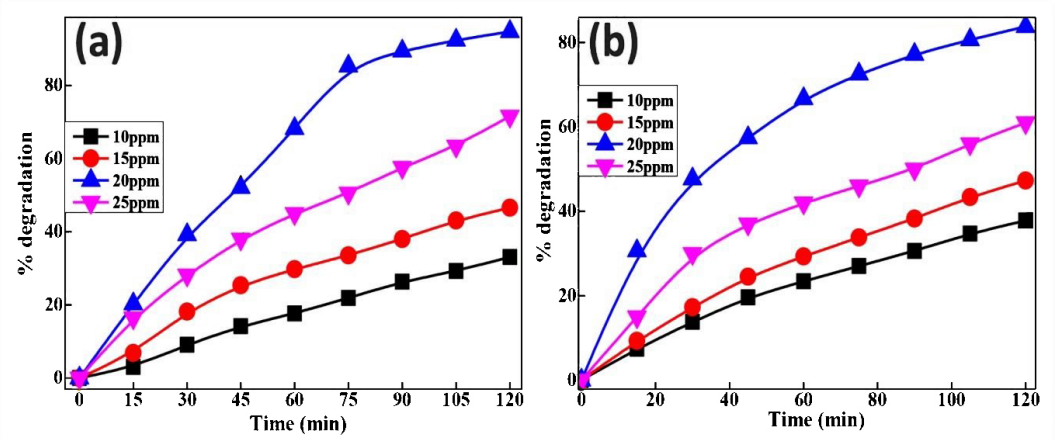

Figure 13. Rate of photodegradation for different ppm of TiO_2 photocatalyst for the decolorization of F-OR under UV and Sunlight illumination.

In addition to destroying the dye, the synthesized sample must to be recyclable and show photostability. This nature was confirmed by running a TiO_2 sample through five cycles of the DG and F-OR dyes at a 20-ppm concentration while exposed to UV and sunshine [39]. When used for repeated cycles following the initial run, the photocatalyst was discovered to be photostable with no change in the decolorization percentage after each cycle, as illustrated in Figures 14 and 15 (a,b). Since nanoparticles were chosen for this work and due to its highly magnetic nature, the photocatalyst was simply removed using a magnet after each cycle [40,41].

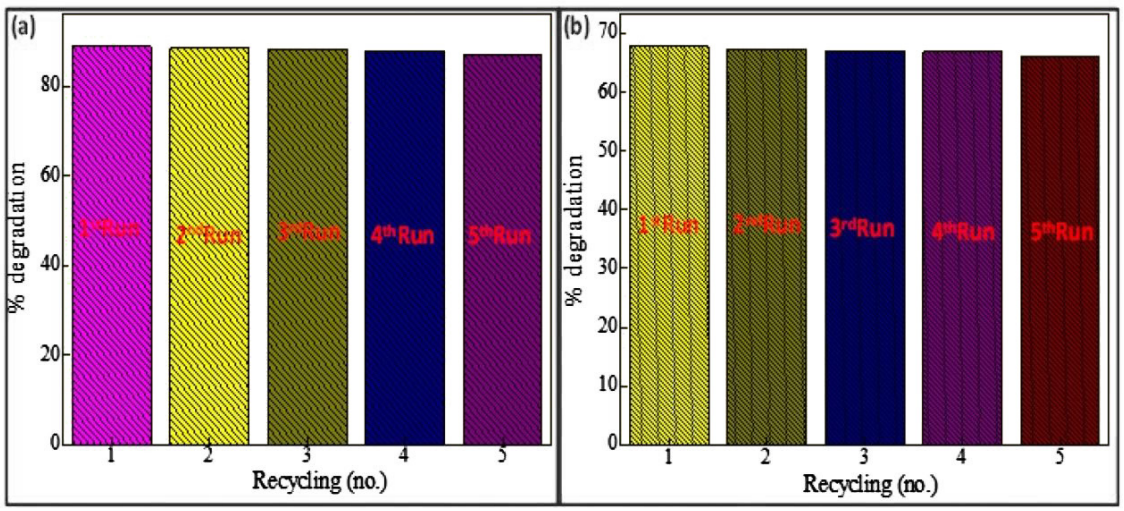

Figure 14. Recyclability of TiO_2 photocatalyst for the decolorization of DG under UV and Sunlight illumination.

https://doi.org/10.61577/jnd.2023.100002

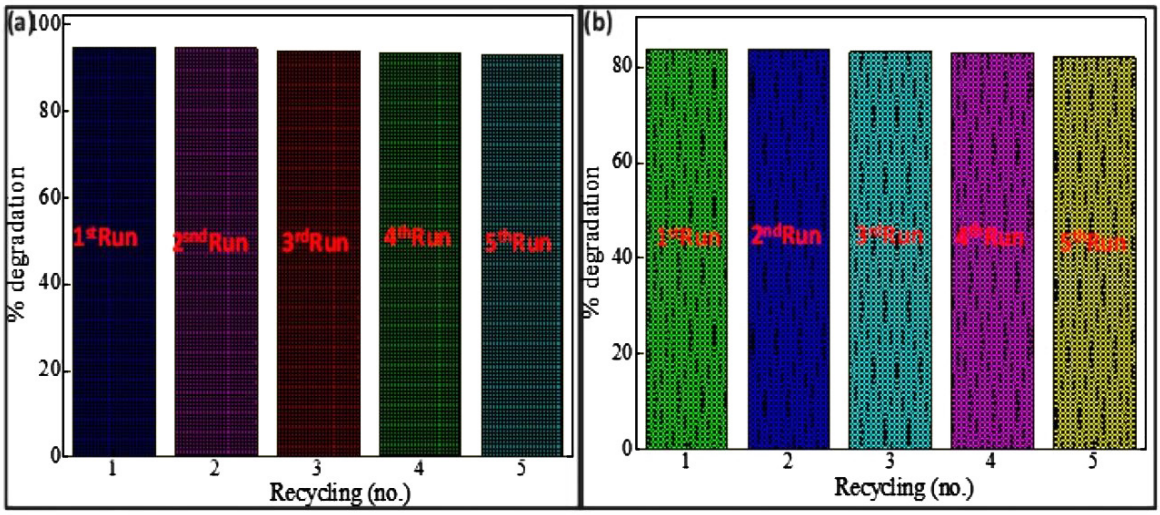

Figure 15. Recyclability of TiO_2 photocatalyst for the decolorization of F-OR under UV and Sunlight illumination.

Scavenging tests were also conducted, as shown in Figures 16 and 17 (a,b), to confirm the photo decolorization capabilities of highly energetic free radicals in the decolorization of DG and F-OR dye in the presence of TiO_2 photocatalyst under UV and sunlight. According to the experimental techniques, the photo decolorization analysis uses three different scavengers, including AgNO3, ethanol, and ethylenediamine tetraacetic acid (EDTA). These three scavengers produce results for DG that are respectively 74.05%, 72.59%, and 68.16% and for F-OR that are 84.13%, 78.21%, and 73.18% under UV light. Thus, due to scavengers inhibiting the electrons, $OH^{\bullet}$ radicals, and holes after 120 min, the experimental photo decolorization results indicated to be 85.3% for DG and 93.8% for F-OR, proving that holes (h^+) are predominantly responsible for photo decolorization [42,43]. Additionally, under sunlight, photo decolorization study using $AgNO_3$, ethanol, and EDTA reveals 57.00%, 51.7%, and 47.5% for DG and 74.4%, 69.37%, and 63.90% for F-OR, respectively. Thus, after 120 minutes, the experimental photo decolorization results for DG and F-OR were 59.9% and 61.7%, respectively. As shown by the said data, UV is a greater decolorizer than sunlight for both DG and F-OR dyes [44,45]. When compared to dyes, F-OR decolorizes clothing more successfully than DG. This clearly shows that TiO_2 has superior photocatalytic action when acting as a catalyst to fade the colour of DG and F-OR in the presence of UV and sunshine. TiO_2 NPs are therefore efficient at treating sewage.

Moreover, the change of optical absorption ability, the formation of N species and defects can be performed using EPR analysis has reported the EPR signal was obtained at g = 2.002 which attributed as an oxygen vacancy with one electron in N doped TiO_2 sample. The oxygen vacancy defects attributed to the visible light absorption, and this will lead to a stability of active nitrogen species. Strong evidence of NPseq-TiO_2 photocatalyst was found where the wavelength has been shifted towards higher wavelength hence so, it activated under visible light energy.

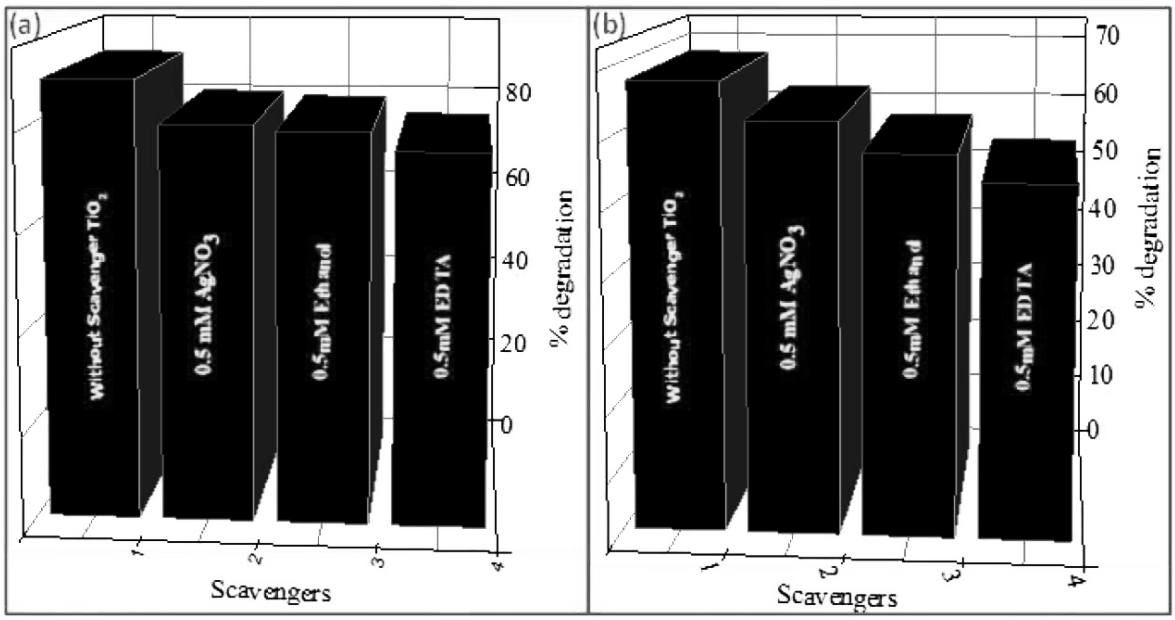

Figure 16. Scavenging examinations of TiO_2 photocatalyst for DG under UV and Sunlight illumination.

https://doi.org/10.61577/jnd.2023.100002

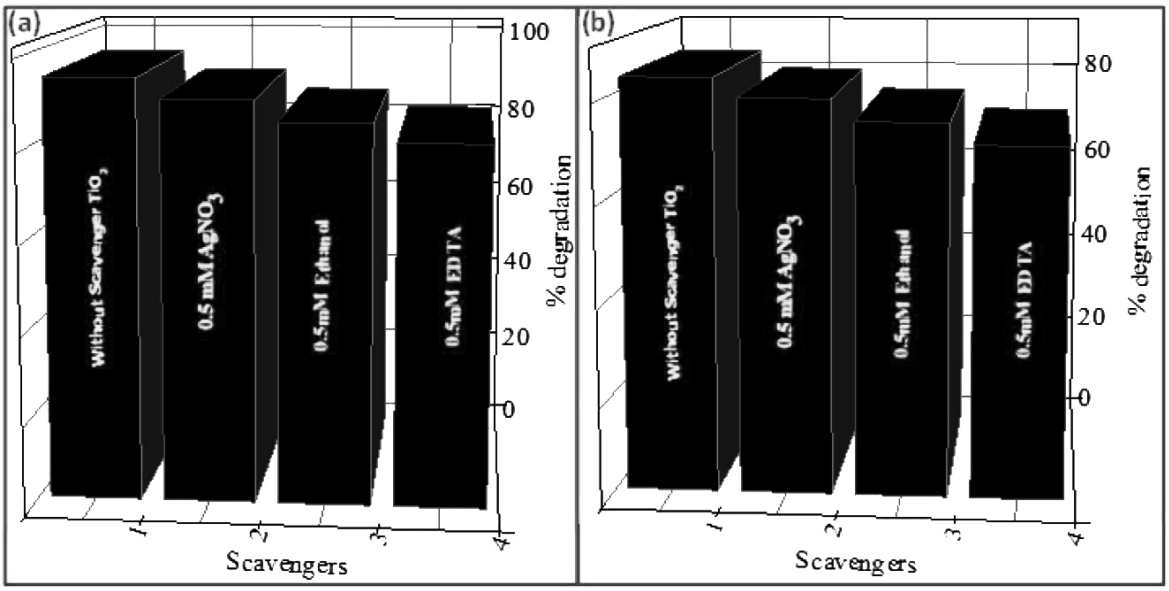

Figure 17. Scavenging examinations of TiO_2 photocatalyst for F-OR under UV and Sunlight illumination.

Electrochemical sensor study

TFigure 18(a) shows the CV curve of CPE using TONP at various scan rates. The cathodic and anodic scans redox peaks demonstrate that pseudo-capacitance contributes significantly to the electrochemical process. The difference between the anodic (E_{pa}) and cathodic (E_{pc}) peak potentials, or E_{ac}, is a clear sign of a redox reaction's reversibility [46]. Correlating the anodic and cathodic peaks to oxidation and reduction potentials, respectively, the Epa, Epc and ΔEa,c value for TiO_2 electrode are calculated. The maximum potential difference Ea,c is only 0.568V. This demonstrates how protons can simply intercalate into the oxide lattice during reduction and out of the oxide lattice during oxidation (reaction 13), allowing for the simple interconversion of oxygen and hydroxide [47].

$$2OH^- \leftrightarrow O_2^{2-} + H_2 \quad (13)$$

The working electrode surface area was calculated with the help of Randles-Sevcik formula [48,49].

$$ip = 2.69 \times 105 \times n^{3/2} \times A \times D^{1/2} \times C0 \times v^{1/2} \quad (14)$$

$K_3Fe(CN)_6$ (1.0×10^{-3} M) was utilized as the test solution and KCl as the supporting electrolyte to determine the surface area (0.1 M). Utilizing the data of diffusion coefficient (D) of 5.9 10-5 cm^2s^{-1} and concentration of test solution(C_0), the number of electrons (n) was calculated to be 1. To do this, use Figure 18a, we displayed the curve of ipa vs. $v^{1/2}$, and from the slope, we computed that the CPE electrode's surface area was 0.045 cm^2 [50].

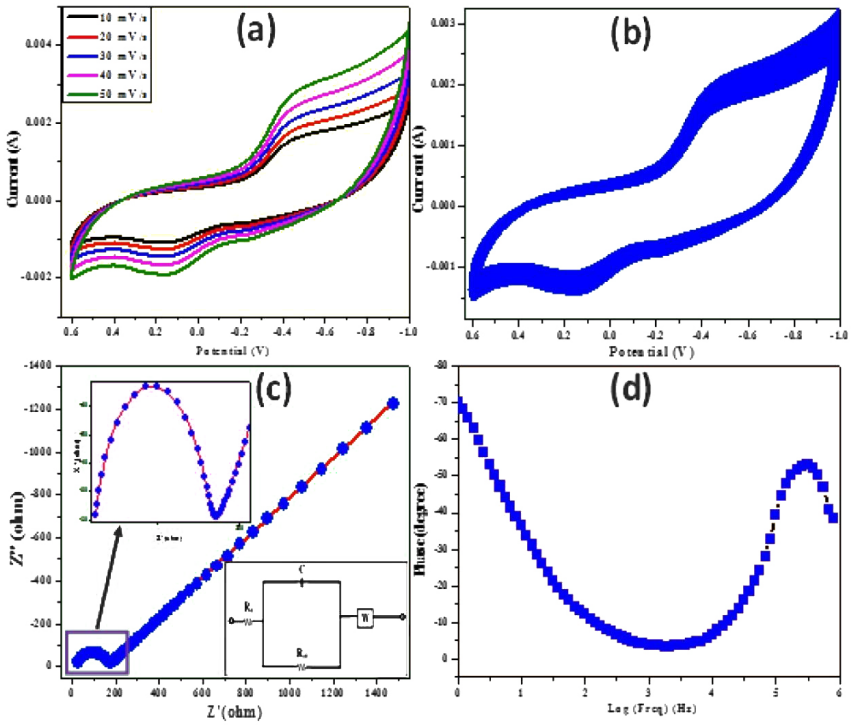

Figure 18. (a) Cyclic voltammogram of CPE using TONPs at different scan rate, (b) CV (50 cycles) at 10 mV/s, (c) Nyquist plot and proposed equivalent circuit and (d) Bode plot of TiO_2 electrode.

https://doi.org/10.61577/jnd.2023.100002

In order to comprehend the electrode stability of the generated oxides, a series of CV scans (of 50 cycles) at a scanning rate of 10 mVs^{-1} were carried out for the TiO_2 electrode (Figure 18(b)). Strong electrode stability is shown by the anodic and cathodic electrode peak sites not changing considerably with growth cycles [51]. The TiO_2 electrode Nyquist plot and equivalent circuit are displayed in the inset of Figure 18(c). The electrode capacitance is represented by a straight line in the low-frequency region of the Nyquist plot, whereas charge transfer at the electrode-electrolyte interface is represented by a high-frequency region that is shown by a semicircle. The diameter of the semicircle arc on the real axis can be determined directly from the charge-transfer resistance RCt [52,53]. Table 1 displays the EIS data derived from the Nyquist plot. The TiO_2 electrode impedance curve is skewed toward the Y axis, which suggests that the produced electrode has a low capacitance and minimal charge-transfer resistance.

Table 1. EIS data of TiO_2 electrode.

Solution resistance (RS) (Ω)	Charge- transfer resistance (RCt) (Ω)	Capacitance of double layer (Cdl) (F)
19.62	184.35	0.000381

Figure 18(d) explains the relation among the phase angle and frequency. It is seen that; the phase angle is -52° which is close for an ideal capacitor (-90°) [54].

The TONPs used to detect lead have cyclic voltammograms, which are shown in Figure19(a). A sharp shift in the locations of the oxidation and reduction peaks suggests that the TONPs used to make the carbon paste electrode are appropriate for use as sensors in acidic media at concentrations of 1 to 5 mM. Additionally, the current response grows with additional injections of 1 mM lead over 50s of sampling time, reaching steady state in under 3s. The anodic oxidation and reduction peaks on the TiO_2 electrode are at 0.167 V and -0.401 V, respectively (Figure 18(a)). On the anodic and cathodic sides of the lead sensor, there are additional peaks on the cyclic voltammogram, with oxidation peaks at 0.104 and 0.48 V and reduction peaks at -0.214 and -0.44 V.

The CV of the TiO_2 electrode in the presence and absence of a lead sensor is shown in Figure 19(b), confirming that the peak positions clearly change when lead is added to the electrolyte.

Figure 19(c), shows the anodic and cathodic current responses in relation to lead concentration. The TiO_2 electrode sensor exhibits an approximately linear trend in with an increase in anodic current at both potentials, but a drop in cathodic current at -0.44 V and an increase at -0.214 V as lead concentration was increased. This further highlights the exceptional sensitivity of the TiO_2-modified electrode to the electrochemical activity of the heavy metal under study.

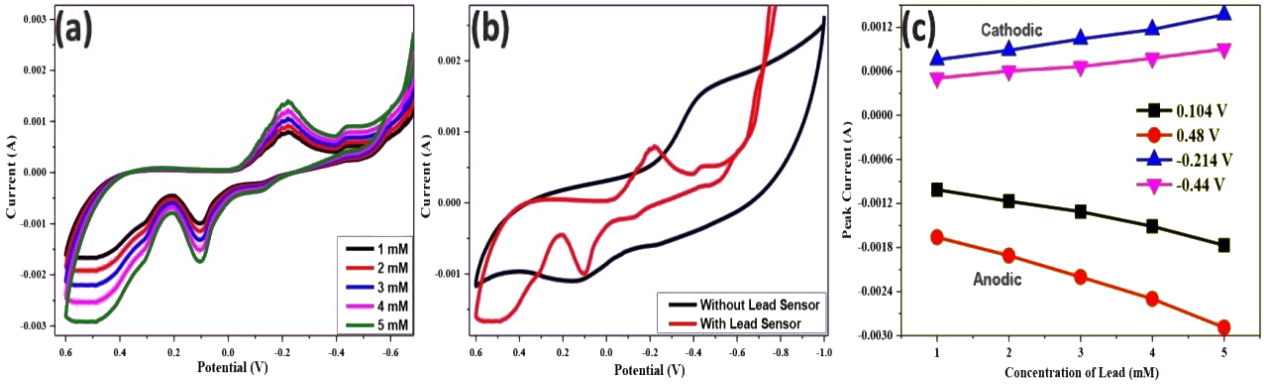

Figure 19. (a) Cyclic voltammogram of CPE electrode TONPs detection of Lead, concentration range 1–5 mM, (b) Cyclic voltammogram of CPE electrode TONPs with and without lead sensor and (c) Peak current vs concentration of Lead.

Repeatability and reproducibility

For 1.0 mM lead, five replications of the CPE electrode TONPs repeatability were examined. For the investigations, the same electrode and standard lead solution were utilized. Using TONPs, the relative standard deviation (RSD) was estimated and found to be 1.6% for CPE. Additionally, for five electrodes made from the same batch of electrode material and used with 1.0 mM lead, the repeatability of the electrode was examined. For CPE employing TONPs, an RSD of 2.08% was noted. The outcomes were satisfactory for CPE as a sensor for lead determination. Further testing of the electrode storage capacity over a period of four weeks revealed no appreciable changes in the lead detection level. The results showed a high lead recovery with a low RSD value, demonstrating the repeatability, reproducibility, and stability of the manufactured electrode and pointing to its possible use as a sensor to measure lead in real sample analysis.

Conclusions

The probe sonication approach was used to successfully create TONPs. According to the PXRD analyses, the substance has an

https://doi.org/10.61577/jnd.2023.100002

anatase structure with an average crystallite size of roughly 39.46 nm. The band gap value for TONPs was 3.26 eV as reported by UV-DRS investigations. After 120 minutes of exposure, TONPs achieved photocatalytic degradation efficiencies for DG and F-OR dyes of 88.9 and 94.75%, respectively, under ultraviolet light. According to the CV study, this electrode was quite effective at finding lead in an acidic solution. The most striking result of the investigation was the quick reactivity of the electrode material (3s), which enabled it to detect the heavy metal at concentrations as low as 1 mM. The decreased charge-transfer resistance value for TONPs, obtained after fitting with the equivalent circuit, was further confirmed by an electrochemical impedance test. The results show that TiO_2 is a ready for commercialization electrode material that is inexpensive and promising for future sensing applications.

Disclosure statement

No potential conflict of interest was reported by the authors.

Authors' contributions

Study conception and design: D.A. Raghupathy; Data collection and editing manuscript: H.C. Ananda Murthy; analysis and interpretation of results: N. Raghavendra and G. Ramgopal; Draft manuscript preparation: C.R. Ravikumar.

Data availability statement

The datasets used and analyzed during the current study are available from the corresponding author on reasonable request.

References

1. Makarov VV, Love AJ, Sinitsyna OV, Makarova SS, Yaminsky IV, Taliansky ME, et al. "Green" nanotechnologies: synthesis of metal nanoparticles using plants. Acta Nat. 2014;6(1):35-44.
2. Jana A, Scheer E, Polarz S. Synthesis of graphene–transition metal oxide hybrid nanoparticles and their application in various fields. Beilstein J Nanotechnol. 2017;8(1):688-714.
3. Kim CS, Moon BK, Park JH, Choi BC, Seo HJ. Solvothermal synthesis of nanocrystalline TiO_2 in toluene with surfactant. J Cryst Growth. 2003;257(3-4):309-315.
4. Gotić M, Musić S. Synthesis of nanocrystalline Iron oxide particles in the Iron(iii) acetate/alcohol/acetic acid system. Eur J Inorg Chem. 2008;6:966-973.
5. Hayashi H, Hakuta Y. Hydrothermal synthesis of metal oxide nanoparticles in supercritical water. Materials. 2010;3:3794-381.
6. Byrne C, Fagan R, Hinder S, McCormack DE, Pillai SC. New approach of modifying the anatase to rutile transition temperature in TiO 2 photocatalysts. RSC Adv. 2016;6(97):95232-95238.
7. Carp O, Huisman CL, Reller A. Photoinduced reactivity of titanium dioxide. Prog Solid State Ch. 2004;32(1-2):33-177.
8. Wang H, Li X, Zhao X, Li C, Song X, Zhang P, et al. A review on heterogeneous photocatalysis for environmental remediation: From semiconductors to modification strategies. Chinese J Catal. 2022;43(2):178-214.
9. Li H, Sun B, Gao T, Li H, Ren Y, Zhou G. Ti3C2 MXene co-catalyst assembled with mesoporous TiO_2 for boosting photocatalytic activity of methyl orange degradation and hydrogen production. Chinese J Catal. 2022;43(2):461-471.
10. Wang J, Wang G, Cheng B, Yu J, Fan J. Sulfur-doped g-C3N4/TiO_2 S-scheme heterojunction photocatalyst for Congo Red photodegradation. Chinese J Catal. 2021;42(1):56-68.
11. Huang J, Li C, Hu X, Fan J, Zhao B, Liu E. K2HPO4-mediated photocatalytic H2 production over NiCoP/RP heterojunction. Chinese J Struc Chem. 2022;41(6):2206062-2206068.
12. Yan T, Zhang X, Liu H, Jin Z. CeO2 particles anchored to Ni2P nanoplate for efficient photocatalytic hydrogen evolution. Chinese J Struc Chem. 2022;41(1):2201047-2201053.
13. Mahlambi MM, Ngila CJ, Mamba BB. Recent developments in environmental photocatalytic degradation of organic pollutants: the case of titanium dioxide nanoparticles-a review. J Nanomater. 2015;2015:1-29.
14. Ahmed MA, El-Katori EE, Gharni ZH. Photocatalytic degradation of methylene blue dye using Fe2O3/TiO_2 nanoparticles prepared by sol–gel method. J Alloys Compd. 2013;553:19-29.
15. Navyashree GR, Nagabhushana H, Sunitha DV, Yeshodamma S. Synthesis of TiO_2 nanoparticles by solution combustion technique using different plant extracts. Int J Eng Res. 2016;50(4):790-991.
16. Thamaphat K, Limsuwan P, Ngotawornchai B. Phase characterization of TiO_2 powder by XRD and TEM. Agric Nat Resour. 2008;42(5):357-361.
17. Rajakumar G, Rahuman AA, Roopan SM, Khanna VG, Elango G, Kamaraj C, et al. Fungus-mediated biosynthesis and characterization of TiO_2 nanoparticles and their activity against pathogenic bacteria. Spectrochim Acta A Mol Biomol Spectrosc. 2012;91:23-29.
18. Kubelka P, Munk F. EinBeitragZur Optic der Farbenstriche. Z Tech Phys. 1931;12:593-601.
19. Anilkumar MR, Nagaswarupa HP, Anantharaju KS, Gurushantha K, Pratapkumar C, Prashantha SC, et al. Green engineered ZnO nanopowders by Banyan Tree and E. tirucalli plant latex: auto ignition route, photoluminescent and photocatalytic properties. Mater Res Express. 2015;2(3):035011.
20. Bouazizi N, Bargougui R, Oueslati A, Benslama R. Effect of synthesis time on structural, optical and electrical properties of CuO nanoparticles synthesized by reflux condensation method. Adv Mater Lett. 2015;6(2):158-164.
21. Rudresha K, Zahir Hussain A, Ravikumar CR, R Anil Kumar M, Nagaswarupa HP, S Santosh M, et al. Synthesis and Characterization of green CuO using Centella Asiatica plant leaf extract: electrochemical and Photocatalytic activities. Adv Mater Lett. 2020;11(12):1-6.
22. Kumar AN, Jnaneshwara DM, Ravikumar CR, Murthy HC, Prashantha SC, Kumar MR, et al. A Comparative Cyclic Voltametric Study on Rare Earth (Eu, Sm, Dy, and Tb) Ions Doped La 10 Si 6 O 27 Nanophosphors for Sensor Application. Adv Mater Sci Eng. 2022;2022.
23. Abebe B, Ravikumar CR, Zereffa EA, Kumar AN, Murthy HA. Photocatalytic and superior ascorbic acid sensor activities of PVA/Zn-Fe-Mn ternary oxide nanocomposite. Inorg Chem Commun. 2021;123:108343.
24. Avinash B, Ravikumar CR, Kumar MA, Santosh MS, Pratapkumar C, Nagaswarupa HP, et al. NiO bio-composite materials: Photocatalytic, electrochemical and supercapacitor applications. Appl Surf Sci Adv. 2021;3:100049.
25. Basavaraju N, Prashantha SC, Nagabhushana H, Naveen Kumar A, Chandrasekhar M, Shashi Shekhar TR, et al. Luminescent and thermal properties of novel orange–red emitting MgNb 2 O 6: Sm 3+ phosphors for displays, photo catalytic and sensor applications. SN Appl Sci. 2021;3:1-5.
26. Ranjitha R, Meghana KN, Kumar VD, Bhatt AS, Jayanna BK, Ravikumar CR, et al. Rapid photocatalytic degradation of cationic organic dyes using Li-doped Ni/NiO nanocomposites and their electrochemical performance. New J Chem. 2021;45(2):796-809.
27. Raghavendra N, Nagaswarupa HP, Shekhar TS, Mylarappa M, Surendra BS, Prashantha SC, et al. Electrochemical sensor studies and optical analysis of developed clay based CoFe2O4 ferrite NPs. Sens. 2021;2:100083.
28. Raj NB, PavithraGowda NT, Pooja OS, Purushotham B, Kumar MA, Sukrutha SK, et al. Harnessing ZnO nanoparticles for antimicrobial and photocatalytic activities. J Photochem Photobiol. 2021;6:100021.
29. Raghavendra N, Nagaswarupa HP, Shekhar TS, Mylarappa M, Surendra BS, Prashantha SC, et al. Development of clay ferrite nanocomposite: electrochemical, sensors and photocatalytic studies. Appl Surf Sci. 2021;5:100103.
30. Kusuma KB, Manju M, Ravikumar CR, Dileepkumar VG, Kumar AN, Santosh MS, et al. Probe sonicated synthesis of bismuth oxide (Bi2O3): photocatalytic application and electrochemical sensing of ascorbic acid and lead. J Nanomater. 2022;2022:1-3.
31. Kumar VD, Balaji KR, Viswanatha R, Ambika G, Roopa R,

https://doi.org/10.61577/jnd.2023.100002

Basavaraja BM, et al. Visible light photodegradation of 2, 4-dichlorophenol using nanostructured NaBiS2: Kinetics, cytotoxicity, antimicrobial and electrochemical studies of the photocatalyst. Chemosphere. 2022;287:132174.
32. Alam MW, Kumar VD, Ravikumar CR, Prashantha SC, Murthy HA, Kumar MA. Chromium (III) doped polycrystalline MgAl2O4 nanoparticles for photocatalytic and supercapacitor applications. J Phys Chem Solids. 2022;161:110491.
33. Mamatha KM, Ravikumar CR, Murthy HA, Kumar VD, Kumar AN, Jahagirdar AA. Facile green synthesis of Molybdenum oxide nanoparticles using Centella Asiatica plant: Its photocatalytic and electrochemical lead sensor applications. Sens. 2022;3:100153.
34. Kumar MA, Abebe B, Nagaswarupa HP, Murthy HA, Ravikumar CR, Sabir FK. Enhanced photocatalytic and electrochemical performance of TiO_2-Fe2O3 nanocomposite: Its applications in dye decolorization and as supercapacitors. Sci Rep. 2020;10(1):1249.
35. Masunga N, Mmelesi OK, Kefeni KK, Mamba BB. Recent advances in copper ferrite nanoparticles and nanocomposites synthesis, magnetic properties and application in water treatment. J Environ Chem Eng. 2019;7(3):103179.
36. Chireh M, Naseri M. Effect of calcination temperature on the physical properties of LiFe5O8 nanostructures. Adv Powder Technol. 2019;30(5):952-960.
37. Fu F, Shen H, Sun X, Xue W, Shoneye A, Ma J, et al. Synergistic effect of surface oxygen vacancies and interfacial charge transfer on Fe (III)/Bi2MoO6 for efficient photocatalysis. Appl Catal B. 2019;247:150-162.
38. Mohamed RM, Ismail AA. Impact of surfactant ratios on mesostructured MnFe2O4 nanocomposites and their photocatalytic performance. Ceram Int. 2020;46(8):10925-10933.
39. Baig MM, Zulfiqar S, Yousuf MA, Touqeer M, Ullah S, Agboola P, et al. Structural and photocatalytic properties of new rare earth La3+ substituted MnFe2O4 ferrite nanoparticles. Ceram Int. 2020;46(14):23208-23217.
40. Yang J, Zhang Y, Zeng D, Zhang B, Hassan M, Li P, et al. Enhanced catalytic activation of photo-Fenton process by Cu0· 5Mn0· 5Fe2O4 for effective removal of organic contaminants. Chemosphere. 2020;247:125780.
41. Meena S, Renuka L, Anantharaju KS, Vidya YS, Nagaswarupa HP, Prashantha SC, et al. Optical, electrochemical and photocatalytic properties of sunlight driven Cu doped manganese ferrite synthesized by solution combustion synthesis. Materials Today: Proceedings. 2017;4(11):11773-11781.
42. Mandal B, Panda J, Paul PK, Sarkar R, Tudu B. MnFe2O4 decorated reduced graphene oxide heterostructures: nanophotocatalyst for methylene blue dye degradation. Vacuum. 2020;173:109150.
43. Boutra B, Güy N, Özacar M, Trari M. Magnetically separable MnFe2O4/TA/ZnO nanocomposites for photocatalytic degradation of Congo Red under visible light. J Magn Magn Mater. 2020;497:165994.
44. Renuka L, Anantharaju KS, Gurushantha K, Nagabhushana H, Vidya YS, Suresh C, et al. Phase-transformation synthesis of Li codoped ZrO2: Eu3+ nanomaterials: Characterization, photocatalytic, luminescent behaviour and latent fingerprint development. Ceram Int. 2021;47(7):10332-10345.
45. Uma B, Anantharaju KS, Renuka L, Nagabhushana H, Malini S, More SS, et al. Controlled synthesis of (CuO-Cu2O) Cu/ZnO multi oxide nanocomposites by facile combustion route: A potential photocatalytic, antimicrobial and anticancer activity. Ceram Int. 2021;47(10):14829-14844.
46. Wang J, Gao Z, Li Z, Wang B, Yan Y, Liu Q, et al. Green synthesis of graphene nanosheets/ZnO composites and electrochemical properties. J Solid State Chem. 2011;184(6):1421-1427.
47. Bouazizi N, Bargougui R, Oueslati A, Benslama R. Effect of synthesis time on structural, optical and electrical properties of CuO nanoparticles synthesized by reflux condensation method. Adv Mater Lett. 2015;6(2):158-164.
48. Prabhu K, Malode SJ, Shetti NP, Kulkarni RM. Analysis of herbicide and its applications through a sensitive electrochemical technique based on MWCNTs/ZnO/CPE fabricated sensor. Chemosphere. 2022;287:132086.
49. Malode SJ, Shetti NP, Reddy KR. Highly sensitive electrochemical assay for selective detection of Aminotriazole based on TiO_2/poly (CTAB) modified sensor. Environ Technol Innov. 2021;21:101222.
50. Shetti NP, Ilager D, Malode SJ, Monga D, Basu S, Reddy KR. Poly (eriochrome black T) modified electrode for electrosensing of methdilazine. Mater Sci Semicond Process. 2020;120:105261.
51. Raghupathy DA, Ramgopal G, Ravikumar CR. Photocatalytic degradation of direct green & fast orange red dyes: Electrochemical sensor of lead using cupric oxide nanoparticles synthesized via sonochemical route. Sens. 2022;3:100204.
52. Girish KM, Prashantha SC, Nagabhushana H, Ravikumar CR, Nagaswarupa HP, Naik R, et al. Multi-functional Zn2TiO4: Sm3+ nanopowders: excellent performance as an electrochemical sensor and an UV photocatalyst. J Sci-Adv Mater Dev. 2018;3(2):151-160.
53. Ashwini R, Dileepkumar VG, Balaji KR, Viswanatha R, Ravikumar CR, Srivastava C, et al. Ternary alkali metal chalcogenide engineered reduced graphene oxide (rGO) as a new class of composite (NaFeS2-rGO) and its electrochemical performance. Sens. 2021;2:100125.
54. Pratapkumar C, Prashantha SC, Nagabhushana H, Anilkumar MR, Ravikumar CR, Nagaswarupa HP, et al. White light emitting magnesium aluminate nanophosphor: near ultra violet excited photoluminescence, photometric characteristics and its UV photocatalytic activity. J Alloys Compd. 2017;728:1124-1138.t

https://doi.org/10.61577/jnd.2023.100002